ARTICLE

Toward High Throughput Interconvertible Graphane-to-Graphene Growth and Patterning

Yu Wang,[†] Xiangfan Xu,[‡] Jiong Lu,[†] Ming Lin,[§] Qiaoliang Bao,[†] Barbaros Özyilmaz,[‡] and Kian Ping Loh[†,*]

[†]Department of Chemistry, National University of Singapore, 3 Science Drive 3, 117543, Singapore, [‡]Department of Physics, National University of Singapore, 2 Science Drive 3, 117542, Singapore, and [§]Institute of Materials Research and Engineering, 3 Research Link, Singapore 117602, Singapore

ABSTRACT We report a new route to prepare high quality, monolayer graphene by the dehydrogenation of graphane-like film grown by plasma-enhanced chemical vapor deposition. Large-area monolayer graphane-like film is first produced by remote-discharged radio frequency plasma beam deposition at 650 °C on Cu/Ti-coated SiO_2—Si. The advantages of the plasma deposition include very short deposition time (<5 min) and a lower growth temperature of 650 °C compared to the current thermal chemical vapor deposition approach (1000 °C). Near edge X-ray adsorption, Raman spectroscopy, and transmission electron microscopy as well as scanning tunneling microscopy have been applied to characterize the graphane-to-graphene transition for the as-deposited films. The fingerprint quantum hall effect of monolayer graphene can be obtained on the fully dehydrogenated graphane-like film; four fully quantized half-integer plateaus are observed. The interconvertibility between graphane-like and graphene here opens up a possible route for the fabrication of regions with varying conductivity in a single deposition system using maskless, laser writing.

KEYWORDS: graphene · graphane · low temperature growth · plasma beam deposition · pattern

Graphene, a single atomic sheet of carbon atoms arranged in a honeycomb lattice, has stimulated intense research interests recently owing to its extremely promising electronic and mechanical properties. Its unique electrical properties are exemplified by electrons behaving like massless Dirac particles, ballistic transport, and room-temperature quantum hall effect.[1−3] To realize the potential of graphene as a post-silicon electronic material, techniques for the large-area synthesis of graphene are needed.[4−6] Beginning with the pioneering work of Rod Ruoff on the CVD deposition of monolayer graphene on copper foil,[7] roll-to-roll processed graphene films can now be produced by chemical vapor deposition on copper foils in a tube furnace operated at 1000 °C.[8] Quantum hall effect and low-temperature mobilities of up to 7350 $cm^2/(V\ s)$ have been observed in these metal-grown graphene films. With the ongoing efforts to improve the sheet conductivity and transparency of CVD graphene, there is a good chance that graphene will replace costly and fragile ITO as the next-generation electrode for solar cell.[9,10]

At present, there is still plenty of room for improving the CVD process in terms of low temperature deposition on soft substrates and synthesis of large area single crystalline graphene films as well as the controlled deposition of bilayer or monolayer thick film. Parallel to the development in large-area growth process, transfer technology for transferring intact films to any desired substrate free from process-related organic residues, wrinkles, and microcracks has to be developed urgently.[11,12] Generally, it is difficult to control the crystalline quality of the copper foil substrate used in CVD, thus grain boundaries and defects on the polycrystalline copper are inevitably inherited by the CVD grown graphene film, which limits the size of the single crystal domains attainable. The high temperature (1000 °C) needed in the thermal decomposition process excludes deposition on many substrates. One strategy is to develop a low temperature CVD process that allows deposition on catalyst-coated substrates. Precracking the gaseous precursors to generate reactive radicals in the pas phase allows the substrate temperature to be lowered. However to date there are no reports of plasma-assisted deposition of large area monolayer graphene films (>1 cm). One reason may be the difficulties in controlling the rate of carbon film deposition, another reason could be the collateral damage caused by energetic plasma ions on the delicate graphene film. In this work, by using a remote-discharged radio frequency atom beam source operating in high vacuum conditions, we have succeeded in preparing large area, uniform, monolayer *hydrogenated graphene* (*i.e.*, graphane-like).

*Address correspondence to chmlohkp@nus.edu.sg.

Received for review July 22, 2010 and accepted September 9, 2010.

Published online September 16, 2010. 10.1021/nn1017389

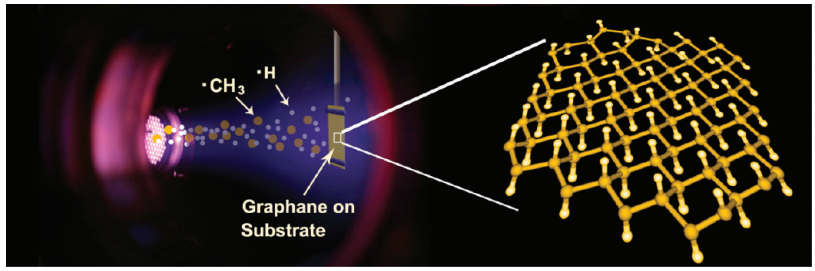

Figure 1. The growth of large-area graphane-like film by RF plasma beam deposition in high vacuum conditions. Reactive neutral beams of methyl radicals and atomic hydrogen effused from the discharged zone and impinged on the Cu/Ti-coated SiO_2/Si samples placed remotely. A substrate heating temperature of 650 °C was applied.

Thermal dehydrogenation of these graphane-like films produces high quality monolayer graphene, as evidenced by the demonstration of the half-integer quantum hall effect. This newly discovered plasma-assisted atom-beam process is important because it opens up a graphane-mediated route to a large area monolayer graphene synthesis at significantly lower temperature compared to the thermal CVD process.

The plasma-assisted deposition of graphane-like film was carried out using a remote-discharged 13.5 MHz radio-frequency plasma beam source mounted in a ultrahigh vacuum (UHV) chamber with a base pressure of 1.0×10^{-9} Torr. The substrate is a 1 cm × 1 cm Ti/Cu (10/500 nm)-coated SiO_2/Si substrate heated by ceramic-coated heating filaments. The Cu catalyst was activated by heating at 600 °C in pure H_2 atmosphere (5.0×10^{-4} Torr). During growth, a premixed gas of 5% CH_4 in H_2 was introduced into the plasma discharge zone and the sample was heated to 650 °C. The atomic beam discharge source produced atomic hydrogen and methyl radicals from these gaseous precursors in the form of a chemical beam. Electrostatically biased deflector plates (+500 V) removed energetic ions effusing from the discharge zone, and neutral species were allowed to impinge on the heated substrate placed at a distance of 12 cm from the beam nozzle. Figure 1 shows a schematic of the plasma beam deposition. Typical deposition time was 5 min. The plasma power was shut off after that, and the sample was allowed to cool to room temperature in vacuum. Due to the presence of excess atomic hydrogen in the gas phase, the deposited film is inevitably hydrogenated.[13] However it is most likely nonstoichiometric in terms of the elemental ratio of C and H, so we denote it as "graphane-like" (or hydrogenated graphene), based on the strict definition of graphane as 1:1 in C:H ratio.

Figure 2a shows a typical optical image of the deposited film transferred onto SiO_2/Si substrate. The

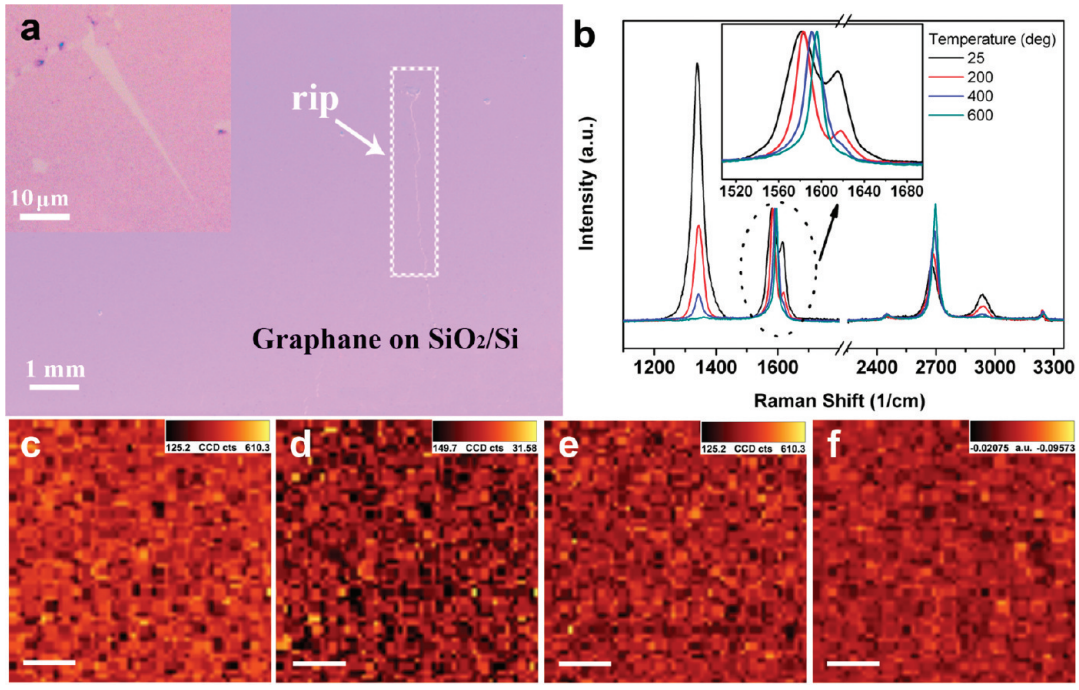

Figure 2. Optical images and Raman measurements of the as-produced graphane-like film. (a) Optical microscope image of the film transferred to a SiO_2/Si substrate. The inset shows ripping along crystallographic directions. (b) The evolution of Raman spectra (532 nm laser wavelength) with increasing annealing temperature for as-produced graphane sample. (c−e) Raman maps of the D(1300−1400), G+D′(1550−1650), and 2D(2650−2750). Scale bar, 4 μm. (f) Optical contrast image shows homogeneous monolayer graphane film. Scale bar, 4 μm.

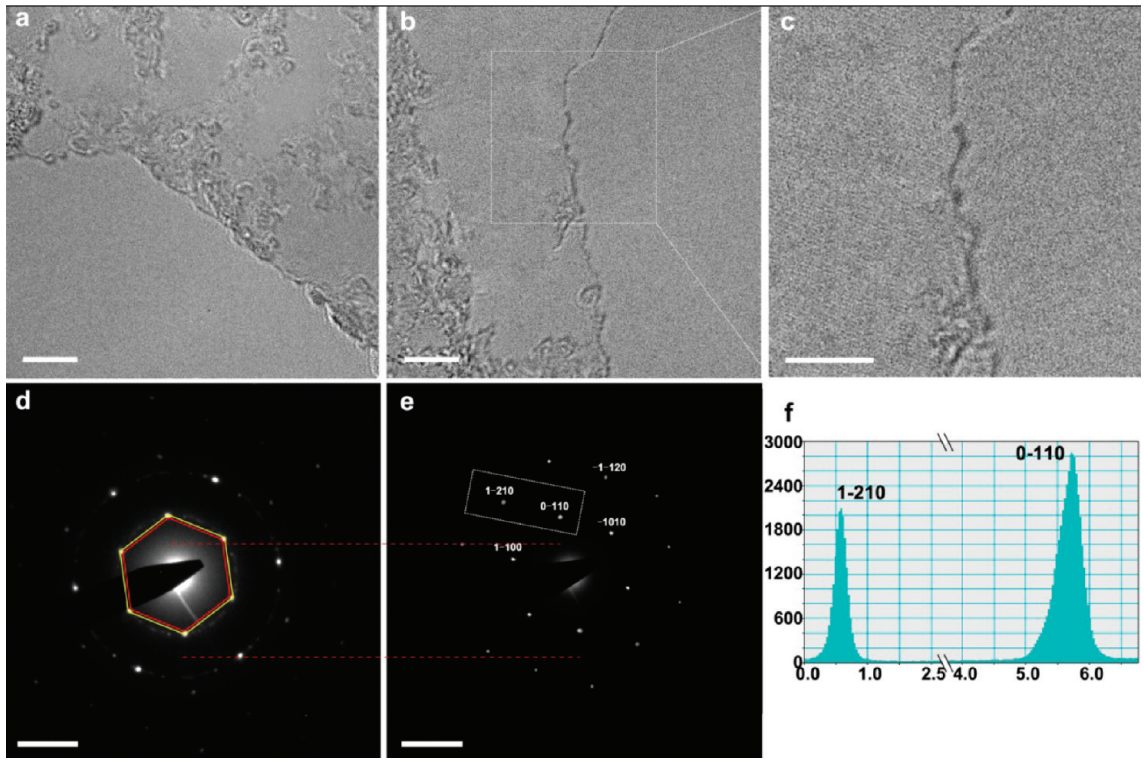

Figure 3. Electron diffraction pattern of graphane, as well as its transformation into graphene after annealing. (a and b) TEM pictures of as-produced graphane and reduced graphene by annealing in 500 °C. (c) A magnifying image of the outlined square in panel b, where regular lattice shows the highly crystalline nature of the graphene sheet derived from graphane. Scale bar, 5 nm. (d) Electron diffraction pattern of graphane-like film synthesized by the plasma beam process. The positions of the diffraction spots in graphane are marked by the yellow hexagon. (e) Graphene, the diffraction spots are corresponding to the red hexagon in panel d. Scale bar, 5 nm^{-1}. (f) Diffraction intensity $I_{(0-110)}/I_{(1-210)}$ is ~1.36 in panel e.

whole sample appears homogeneous except for the presence of some ruptured region during the transfer process. Raman measurements were carried out at different positions in order to analyze the spatial uniformity of the samples. The Raman spectrum of the deposited film is shown in Figure 2b. The spectrum shows a marked resemblance to the spectrum of hydrogenated graphene obtained by the hydrogenation of mechanically cleaved graphene (Supporting Information, S1). Both spectra are characterized by the presence of a disorder-induced D peak at around 1345 cm^{-1}. A shoulder peak of G-band (1580 cm^{-1}), called D′ band, appears at 1620 cm^{-1}. This originates from an intervalley double-resonance Raman process, where the associated phonons have small wavevectors in the vicinity of the Γ point.[14] A peak, which can be assigned to the combination of D mode and G mode, can be found around 2935 cm^{-1}. To investigate if the CVD graphane-like film can be transformed into graphene, the evolution of these Raman peaks at different stages of thermal annealing were monitored. With increasing annealing temperature, we observed a decrease of the I_D/I_G ratio and the shift of the G band toward higher frequencies (Figure 2b, inset). This is accompanied by a reduction of the full width-at-half-maximum (fwhm) of the Raman peak. These changes reflect an increase in the number of sp^2 domains. The gradual disappearance of D′ peak and D+G peak indicates graphane is turning into graphene by dehydrogenation. Finally the spectrum resembles that of mechanically exfoliated graphene, as shown; the fwhm of the 2D peak is ~29 cm^{-1}, which is characteristic of monolayer film (or at least uncoupled monolayers in few layered films).[15]

The homogeneity of the sample can be assessed using Raman mapping. Figure 2 panels c−e present the Raman mapping images of the D, G+D′, and 2D band. The uniform intensity distribution demonstrates that the graphane-like sample is homogeneous in thickness. Using optical contrast technique, the thickness of a graphene sheet can be determined directly by comparing the contrast value with the standard values.[16,17] The contrast spectra $C(\lambda)$ are defined using $C(\lambda) = [R_0(\lambda) - R(\lambda)]/R_0(\lambda)$, where $R_0(\lambda)$ is the reflection from SiO_2/Si and $R(\lambda)$ is reflection from graphene sheets. The contrast values of graphene on SiO_2 substrate are found to be around $N \times (-0.068)$ for N ($N = 1, 2, 3, ...$) layers of graphene. From contrast spectra, the contrast value of the CVD graphane-like film is calculated to be less than −0.1, indicating that the graphane-like film is monolayer thick (Figure 2f).

Transmission microscopy analysis of the graphane-like film, as shown in Figure 3a, reveals 6- fold symmetry diffraction spots superimposed on weak traces of polycrystalline rings which may have come from hydro-

genated domains with disrupted long-range crystallinity. The electron diffraction spots in Figure 3d are labeled using Miller−Bravais (*hkl*) indices. After the thermal annealing of the graphane-like films to 500 °C, a clear 6-fold symmetry diffraction image is observed in Figure 3e. Monolayer film is distinguished by a stronger diffraction intensity from the $(0\bar{1}10)$ plane compared to the $(1\bar{2}10)$ plane, and the reverse is true for bilayer or trilayer graphene films. Indeed, the analysis of the diffraction intensity ratio of the two planes reveals a ratio of 1.36 for $I(0\bar{1}10)/I(1\bar{2}10)$, which is consistent with diffraction from monolayer film (Figure 3f). The graphane-like film has a slightly contracted in-plane bonding compared to graphene, following the annealing of the film, the unit cell increases 1.6% to ~2.46 Å, which agrees with the theoretical calculation and experimental results for graphane-to-graphene conversion.[13,18]

The polarization-dependent near-edge X-ray absorption fine structure (NEXAFS) spectra C *K*-edge were recorded to examine the evolutions of π*and σ* resonance following the dehydrogenation of the graphane-like film. The NEXAFS spectrum of CVD deposited graphane-like film resembles that of a hydrocarbon, and the energy range can be broadly subdivided into the first sharp π* resonance around 284.5 eV, the C−H* resonance around 288 ± 1 eV, and a broad σ* region between 290−315 eV.[19,20] The π* resonance is associated with the conduction π states around the *M* and *L* points of the Brillouin Zone (BZ). Compared to pure graphene, the π* peaks resonance in our CVD graphane-like film is much weaker in intensity due to the conversion of some sp^2 to sp^3 bonded phases. Toward the higher energy shoulder of the sharp π* peak, structures associated with C1s → σ* (C−H or C−C) transitions can be seen at 289 and 293 eV.[21] Following thermal annealing to 600 °C, these C−H or σ* related features attenuate in intensity and what remains is a sharp π* resonance peak, which evidences the recovery of extended π conjugation in the film.

To examine the distribution of adsorbed hydrogen on the graphane-like films, we deposited the graphane-like films on ruthenium crystal and recorded the evolution of the STM images as the sample was annealed to different temperature. In parallel with NEXAFS results, the adsorbate structures of atomic hydrogen on the basal plane of graphane-like film were investigated as a function of annealing temperature in order to gain insight into preferential adsorption, clustering, and desorption on the surfaces. Monolayer graphene usually displays a characteristic moiré superlattice on ruthenium, but a high coverage of hydrogen adsorbates on the graphane surface prevents a clear view of the moiré superlattice. As shown in Figure 4d, a number of bright protrusions are distributed randomly on the as-grown graphane-like film, which indicates that larger hydrogen clusters are formed.[22,23] After annealing at 300 °C

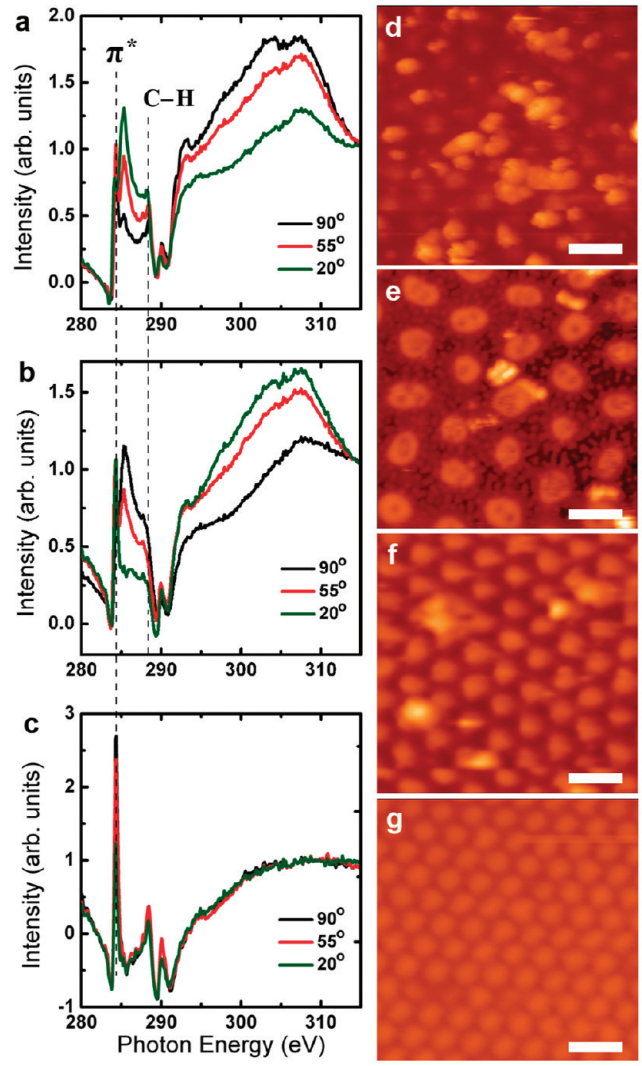

Figure 4. Polarized NEXAFS C K-edge spectra and STM images showing the transformation of graphane-like film to graphene by annealing. (a−c) Polarized NEXAFS C K-edge spectra of graphane film with different annealing temperature: (a) hydrogen-saturated graphane, (b) annealed to 300 °C, (c) annealed to 600 °C. All spectra have been pre- and postedge normalized. (d) STM images of graphane. The bright protrusions in the image are identified as atomic hydrogen clusters (imaging parameters: V_t = 3 V, I_t = 0.11 nA); (e) after annealing at 300 °C for 20 min (imaging parameters: V_t = 1.20 V, I_t = 0.10 nA); (f) after annealing at 400 °C for 20 min (imaging parameters: V_t = 0.5 V, I_t = 0.08 nA); (g) graphene recovered from graphane after annealing to 600 °C for 20 min (imaging parameters: V_t = 0.6 V, I_t = 0.23 nA). Scale bar, 3 nm.

for 20 min, regular ringlike protrusions are observed at the bright moiré regions where the film is lifted from Ru substrate (Figure 4e), which indicates that the hump rather than the valley region of moiré superlattice acts as a sink for diffusing hydrogen atoms. In the ringlike graphane islands on the moiré hump, adjacent carbon atoms may be bound to hydrogen atoms above and below the plane, resulting in a rehybridization from sp^2 to sp^3 bonding. Figure 4f shows the surface of the film after annealing to 400 °C for 20 min. The reduction in the number of bright protrusions suggests that hydrogen clusters are bound weakly. After annealing to 600 °C, the complete recovery of the characteristic Moiré su-

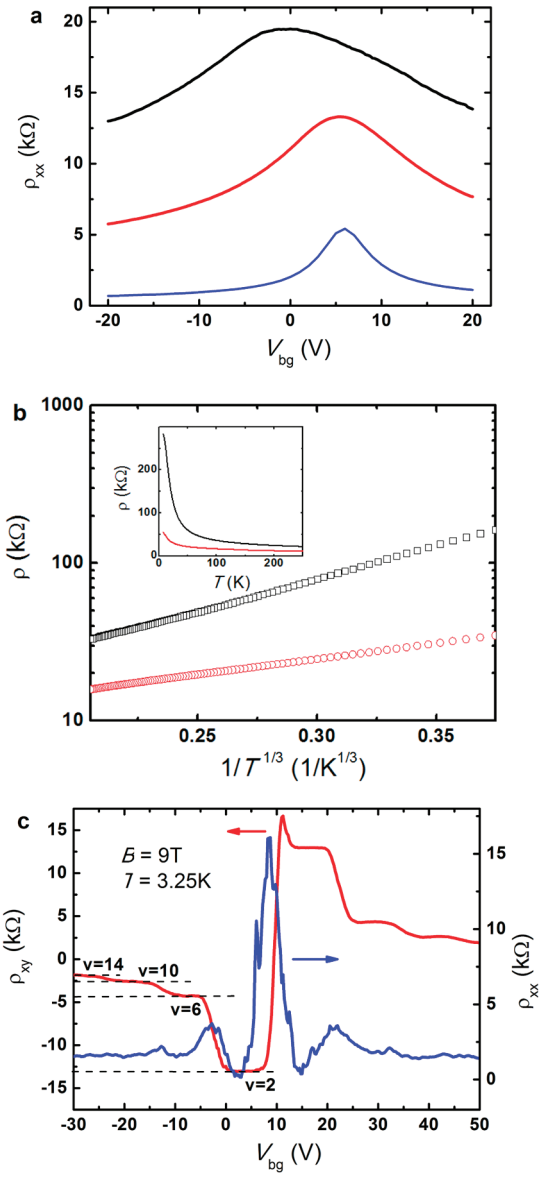

Figure 5. Electrical transport characterizations of the graphene with different amount of hydrogen. (a) The field effect at room temperature with $B = 0$ T for as-prepared (black curve) graphane-like monolayer, partially dehydrogenated (red curve), and fully dehydrogenated graphane (blue curve). (b) Temperature dependence of resistivity at the charge neutral point for partially hydrogenated (red curve) and fully hydrogenated graphane (black curve). (c) Quantum Hall effect at $T = 3.25$ K and $B = 9$ T for the dehydrogenated graphane. The first four half-integer plateaus with $\nu = 2$, 6, 10, and 14, which is the fingerprint of single-layer graphene, are clearly observed.

perlattice for graphene on Ru (0001) can be seen in Figure 4g.

Electronic transport measurements were carried out on the as-grown CVD graphane-like film, as well as partially dehydrogenated and fully dehydrogenated graphane films. The as-grown graphane-like samples show standard bipolar field effect (Figure 5a) with a field-effect mobility of 360 cm^{-2}/(V s) and 150 cm^{-2}/(V s) in partially hydrogenated and hydrogen-saturated graphane samples, respectively. The resistivity of the hydrogen-saturated graphane increases by more than an order of magnitude when the temperature changes from 25K to 7 K (insert of Figure 5b), indicating a semiconductor-like behavior. The observed temperature dependent resistivity $\rho(T)$ can be fitted by $\exp[(T_0/T)^{1/3}]$, which is the characteristic behavior of 2D variable-range hopping system. T_0 reaches as high as 97 and 750 K for partially hydrogenated and hydrogen-saturated graphene, respectively.

The dehydrogenated graphane-like film exhibits a field-effect mobility of ~3420 cm^{-2}/(V s) (blue curve in Figure 5a). The high mobility allows the observation of the graphene specific quantum Hall effect (QHE). We can access the quantum Hall state when tuning the electron density by adjusting the gate voltage V_g at high magnetic field and low temperature. The QHE is measured at $B = 9$ T and $T = 3.2$ K. The longitudinal resistivity ρ_{xx} and Hall resistivity ρ_{xy} are plotted as a function of gate voltage in Figure 5c. A series of half-integer plateaus with an integer filling factor $\nu = 2$, 6, 10, and 14, are clearly observed, which are the hallmark of the monolayer graphene. These QHE effects are not present in the graphane-like film and only appear when it is fully dehydrogenated. The QHE also provides clear verification of the monolayer characteristic of our fully dehydrogenated graphane-like film which has now become graphene.[1,3] The high mobility and QHE provides evidence for the high quality of the derived graphene. It provides further affirmation that the hydrogenation process is reversible on the chemically robust graphene platform, which allows reversible tuning of the metallic-semiconductor characteristics.

The ready conversion of graphane-like film into graphene film provides the conceptual basis for designing an *in situ* "grow-and-pattern" process. The remote-discharged plasma beam source can be incorporated together with a laser microstructuring system in a single chamber for simultaneous "grow-and-pattern" process (Figure 6a). By moving the computer-controlled sample stage in a programmable step with respect to the focused laser beam, patterns with tunable width and length could be directly written (Figure 6b,e) on the graphane-like film. When the focused laser beam was incident on the graphane-like film, the irradiated area absorbed the laser energy, and laser-induced desorption of hydrogen can occur. Raman mapping of the D band (Figure 6c,f) shows a reduction in intensity (dark contrast) after the laser irradiation. As shown in Figure 6d, the laser-irradiated regions show significantly reduced defect bands (D and D′), which reflect that the irradiated regions undergo an annealing process and recovery of sp^2 conjugation. This suggests that the graphane-like film can be directly dehydrogenated by a maskless process using laser annealing to produce graphene ribbons or squares. It should be possible to produce a metal−semiconductor junction in this manner.

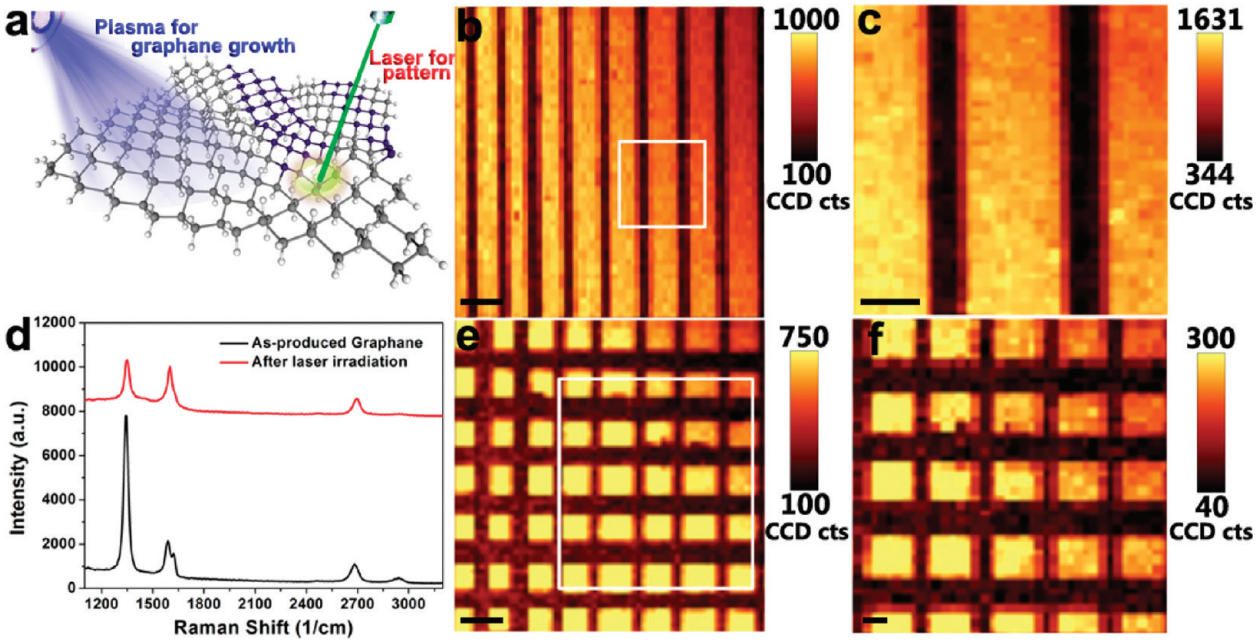

Figure 6. A maskless laser writing process for the dehydrogenation of graphane-like film: (a) Schematic illustration of the *in situ* "grow- and pattern" process. (b and e) 2D Raman mapped images of the graphane-like ribbon and square, respectively. The dark region corresponds to the laser irradiated area, showing the conversion from the graphane-like to graphene. Scale bar, 10 μm. (c and f) Magnified images of the white square region of panels b and e, respectively. Scale bar, 4 μm. (d) Raman spectra of the region before and after laser writing. It is clear that H-related defects peaks such as D band at 1345 cm^{-1} and D'' band at 1620 cm^{-1} have attenuated significantly after laser-irradiation.

In conclusion, we have demonstrated a plasma deposition process for preparing monolayer graphene using graphane-like film as an intermediate phase. The advantage of the plasma deposition process is that it is inherently compatible with wafer-scale processing and lithographical patterning as well as deposition on metal-coated silicon substrates at temperature (at least 350 °C lower) lower than that used in thermal CVD processes. An extensive range of characterization techniques ranging from atomic imaging to electrical transport measurements prove that the as-deposited monolayer graphane-like film can be converted to graphene without compromising the crystalline integrity of the films. The plasma CVD process is easily amenable to the chemical tailoring of carbon films. In addition, this method has the potential to prepare monolayer variants such as monolayer fluorinated graphene films (using CF_4, *etc.*) and monolayer boron nitride films. The combination of noncontact direct write technique together with the plasma beam deposition has great potential to emerge as a high throughput, parallel processing technique for the simultaneous or sequential growth and patterning of graphene. The direct-write process reduces the number of masking or photoresist steps needed when designing an integrated circuit based on all-carbon electronics.

METHODS

Characterization. The as-produced graphane-like and graphene films were characterized using high-resolution transmission electron microscopy (HR-TEM, FEI Titan, 80 kV). After TEM images were obtained, selected area electron diffraction was used to distinguish the molecular structure difference between graphane and graphene. The Raman spectra were measured with a WITEC CRM200 Raman system at room temperature. The excitation source is a 532 nm laser (2.33 eV) with a laser power below 0.1 mW to avoid laser induced heating of the sample. The spot sizes of 532 nm laser and white light are estimated to be 500 nm and 1 μm, respectively. For the contrast and Raman image, the sample was placed on an $x-y$ piezostage and scanned under the illumination of laser and white light. The Raman and reflection spectra from every spot of the sample were recorded.

For the resistance measurement, we apply a small AC current (10 nA) on the samples and measure longitudinal and transverse voltage using Stanford 830 lock-in amplifier. The samples were made into Hall bar geometry by a standard e-beam lithography technique with the length of 3.5 μm between source and drain. Highly doped silicon wafer is used as the gate electrode with a 300 nm silicon oxide as the dielectric layer. The charge density in graphene is induced by applying a gate voltage through a Keithley 6430 DC current source. The room temperature resistance is measured in a probe station (Alessi REL-4800). Low temperature magnetoresistance is measured in a Cryogenic 9T High Field System with a temperature range from 3 to 300 K.

Laser Pattern. The optical microscope-focused laser beam setup was described in our previous study.[24] The laser beam was focused with a 100× objective lens. The laser used was a continuous wave diode laser with wavelength of 532 nm and a maximum output power of ~330 mW. The laser beam was directed toward the objective lens of the microscope *via* a beam splitter and was focused tightly onto the graphane-like samples. The scan rate of the laser beam on substrate is 5 μm/s, and the laser beam diameter is around 1 μm. The

sample was mounted on a computer controlled $x-y$ motorized stage such that during the process of laser patterning the film was moved relative to the focused laser beam.

Acknowledgment. We thank the financial supports from NRF-CRP award "Graphene and Related Materials and Devices R-143-000-360-281'', NRF RF Award No. NRFRF2008-07 ONR Award, and by NUS NanoCore.

Supporting Information Available: A detailed description of the experimental methods and additional experimental results. This material is available free of charge *via* the Internet at http://pubs.acs.org.

REFERENCES AND NOTES

1. Novoselov, K. S.; Geim, A. K.; Morozov, S. V.; Jiang, D.; Katsnelson, M. I.; Grigorieva, I. V.; Dubonos, S. V.; Firsov, A. A. Two-Dimensional Gas of Massless Dirac Fermions in Graphene. *Nature* **2005**, *438*, 197–200.
2. Novoselov, K. S.; Geim, A. K.; Morozov, S. V.; Jiang, D.; Zhang, Y.; Dubonos, S. V.; Grigorieva, I. V.; Firsov, A. A. Electric Field Effect in Atomically Thin Carbon Films. *Science* **2004**, *306*, 666–669.
3. Zhang, Y. B.; Tan, Y. -W.; Stormer, H. L.; Kim, P. Experimental Observation of the Quantum Hall Effect and Berry's Phase in Graphene. *Nature* **2005**, *438*, 201–204.
4. Kim, K. S.; Zhao, Y.; Jang, H.; Lee, S. Y.; Kim, J. M.; Kim, K. S.; Ahn, J.-H.; Kim, P.; Choi, J.-Y.; Hong, B. H. Large-Scale Pattern Growth of Graphene Films for Stretchable Transparent Electrodes. *Nature* **2009**, *457*, 706–710.
5. Zhu, Y.; Murali, S.; Cai, W.; Li, X.; Suk, J. W.; Potts, J. R.; Ruoff, R. S. Graphene and Graphene Oxide: Synthesis, Properties, and Applications. *Adv. Mater.* **2010**, *22*, 3905–3924.
6. Reina, A.; Jia, X.; Ho, J.; Nezich, D.; Son, H.; Bulovic, V.; Dresselhaus, M. S.; Kong, J. Large Area, Few-Layer Graphene Films on Arbitrary Substrates by Chemical Vapor Deposition. *Nano Lett.* **2009**, *9*, 30–35.
7. Li, X. S.; Cai, W. W.; An, J. H.; Kim, S.; Nah, J.; Yang, D. X.; Piner, R.; Velamakanni, A.; Jung, I.; Tutuc, E.; *et al*. Large-Area Synthesis of High-Quality and Uniform Graphene Films on Copper Foils. *Science* **2009**, *324*, 1312–1314.
8. Bae, S. K.; Kim, H. K.; Lee, Y.; Xu, X. F.; Park, J. S.; Zheng, Y.; Balakrishnan, J.; Lei, T.; Kim, H. R.; Song, Y.; *et al*. Roll-to-Roll Production of 30-Inch Graphene Films for Transparent Electrodes. *Nat. Nanotechnol.* **2010**, *5*, 574–578.
9. Wang, X.; Zhi, L. J.; Müllen, K. Transparent, Conductive Graphene Electrodes for Dye-Sensitized Solar Cells. *Nano Lett.* **2008**, *8*, 323–327.
10. Wang, Y.; Chen, X. H.; Zhong, Y. L.; Zhu, F. R.; Loh, K. P. Large Area, Continuous, Few-Layered Graphene as Anodes in Organic Photovoltaic Devices. *Appl. Phys. Lett.* **2009**, *95*, 063302.
11. Li, X. S.; Zhu, Y. W.; Cai, W. W.; Borysiak, M.; Han, B. Y.; Chen, D.; Piner, R. D.; Colombo, L.; Ruoff, R. S. Transfer of Large-Area Graphene Films for High-Performance Transparent Conductive Electrodes. *Nano Lett.* **2009**, *9*, 4359–4363.
12. Caldwell, J. D.; Anderson, T. J.; Culbertson, J. C.; Jernigan, G. G.; Hobart, K. D.; Kub, F. J.; Tadjer, M. J.; Tedesco, J. L.; Hite, J. K.; Mastro, M. A.; *et al*. Technique for the Dry Transfer of Epitaxial Graphene onto Arbitrary Substrates. *ACS Nano* **2010**, *4*, 1108–1114.
13. Elias, D. C.; Nair, R. R.; Mohiuddin, T. M. G.; Morozov, S. V.; Blake, P.; Halsall, M. P.; Ferrari, A. C.; Boukhvalov, D. W.; Katsnelson, M. I.; Geim, A. K.; *et al*. Control of Graphene's Properties by Reversible Hydrogenation: Evidence for Graphane. *Science* **2009**, *323*, 610–613.
14. Saito, R.; Jorio, A.; Souza Filho, A. G.; Dresselhaus, G.; Dresselhaus, M. S.; Pimenta, M. A. Probing Phonon Dispersion Relations of Graphite by Double Resonance Raman Scattering. *Phys. Rev. Lett.* **2001**, *88*, 027401.
15. Casiraghi, C.; Pisana, S.; Novoselov, K. S.; Geim, A. K. Raman Fingerprint of Charged Impurities in Graphene. *Appl. Phys. Lett.* **2007**, *91*, 233108.
16. Ni, Z. H.; Wang, H. M.; Kasim, J.; Fan, H. M.; Yu, T.; Wu, Y. H.; Feng, Y. P.; Shen, Z. X. Graphene Thickness Determination Using Reflection and Contrast Spectroscopy. *Nano Lett.* **2007**, *7*, 2758–2763.
17. Bao, Q. L.; Zhang, H.; Wang, Y.; Ni, Z. H.; Yan, Y. L.; Shen, Z. X.; Loh, K. P.; Tang, D. Y. Atomic-Layer Graphene as a Saturable Absorber for Ultrafast Pulsed Lasers. *Adv. Funct. Mater.* **2009**, *19*, 3077–3083.
18. Ryu, S.; Han, M. Y.; Maultzsch, J.; Heinz, T. F.; Kim, P.; Steigerwald, M. L.; Brus, L. E. Reversible Basal Plane Hydrogenation of Graphene. *Nano Lett.* **2008**, *8*, 4597–4602.
19. Hoffman, A.; Comtet, G.; Hellner, L.; Dujardin, G.; Petravic, M. Surface Near-Edge X-ray Adsorption Fine Structure of Hydrogenated Diamond Films and C(100) Surfaces Studied by H^+ and H^- Ion Desorption. *Appl. Phys. Lett.* **1998**, *73*, 1152.
20. Laikhtman, A.; Gouzman, I.; Hoffman, A. NEXAFS Spectroscopy of Crystalline and Ion Beam Irradiated Diamond Surfaces. *Diamond. Relat. Mater.* **2000**, *9*, 1026–1031.
21. Fayette, L.; Marcus, B.; Mermoux, M.; Tourillon, G.; Laffon, K.; Parent, P.; Normand, F. L. Local Order in CVD Diamond Films: Comparative Raman, X-ray-Diffraction, and X-ray-Absorption Near-Edge Studies. *Phys. Rev. B* **1998**, *57*, 14123.
22. Hornekœr, L.; Šljivančanin, Ž.; Xu, W.; Otero, R.; Rauls, E.; Lœgsgaard, E.; Hammer, B.; Besenbacher, F. Metastable Structures and Recombination Pathways for Atomic Hydrogen on the Graphite (0001) Surface. *Phys. Rev. Lett.* **2006**, *96*, 156104.
23. Balog, R.; Jørgensen, B.; Wells, J.; Lœgsgaard, E.; Hofmann, P.; Besenbacher, F.; Hornekœr, L. Atomic Hydrogen Adsorbate Structures on Graphene. *J. Am. Chem. Soc.* **2009**, *131*, 8744–8745.
24. Zhou, Y.; Bao, Q. L.; Varghese, B.; Tang, L. A. L.; Tan, C. K.; Sow, C.-H.; Loh, K. P. Microstructuring of Graphene Oxide Nanosheets Using Direct Laser Writing. *Adv. Mater.* **2010**, *22*, 67–71.